ROYAL SOCIETY OF CHEMISTRY

PAPER

Check for updates

Vapor growth of binary and ternary phosphorus-based semiconductors into TiO$_2$ nanotube arrays and application in visible light driven water splitting†

Ebru Üzer, [ID] [a] Pawan Kumar, [ID] ‡[b] Ryan Kisslinger,‡[b] Piyush Kar,[b] Ujwal Kumar Thakur,[b] Karthik Shankar [ID] *[b] and Tom Nilges [ID] *[a]

We report successful synthesis of low band gap inorganic polyphosphide and TiO$_2$ heterostructures with the aid of short-way transport reactions. Binary and ternary polyphosphides (NaP$_7$, SnIP, and (CuI)$_3$P$_{12}$) were successfully reacted and deposited into electrochemically fabricated TiO$_2$ nanotubes. Employing vapor phase reaction deposition, the cavities of 100 μm long TiO$_2$ nanotubes were infiltrated; approximately 50% of the nanotube arrays were estimated to be infiltrated in the case of NaP$_7$. Intensive characterization of the hybrid materials with techniques including SEM, FIB, HR-TEM, Raman spectroscopy, XRD, and XPS proved the successful vapor phase deposition and synthesis of the substances on and inside the nanotubes. The polyphosphide@TiO$_2$ hybrids exhibited superior water splitting performance compared to pristine materials and were found to be more active at higher wavelengths. SnIP@TiO$_2$ emerged to be the most active among the polyphosphide@TiO$_2$ materials. The improved photocatalytic performance might be due to Fermi level re-alignment and a lower charge transfer resistance which facilitated better charge separation from inorganic phosphides to TiO$_2$.

1. Introduction

Depleting fossil fuel reserves and rising atmospheric greenhouse gas concentration have motivated the search for new energy sources. Using sunlight as the energy source to generate hydrogen from water through water splitting is an enticing approach. Hydrogen is considered a clean fuel with a high calorific value; it can be stored in a solid/liquid adsorbent or transformed into hydrocarbons using CO$_2$ to produce a syngas mixture. Many photocatalytic materials such as ZnO, CdS, ZnS, InVO$_4$, AgPO$_4$, SrTiO$_3$ and TaON have been widely investigated to achieve water splitting.[1–4] TiO$_2$ has proven to be an excellent photocatalytic material due to its promising band edge potential, non-toxic and non-corrosive nature, and earth-abundance. However, issues such as its large band gap, less reductive conduction band, short lived charged carriers and poor quantum efficiency are the main obstacles preventing the successful deployment of sustainable photocatalysts.[5–7] Hybridization of TiO$_2$ with various low band gap

semiconductors to produce direct/Z-scheme photocatalysts, doping, sensitization, formation of Schottky junctions and nanoscale structural modification (*i.e.,* nanotubes/nanorods/nanospikes/nanospheres) have proven to enhance photocatalytic performance and/or charge separation.[8–13] Polyphosphides are an intriguing class of low band gap semiconductors for this purpose.[14,15] We selected three polyphosphides, namely NaP$_7$, SnIP (ranging from 1.71–1.86 eV)[16–18] and (CuI)$_3$P$_{12}$ (2.84 eV, own measurement see below) because of their different band gaps and their ability to be synthesized in a mineralizer-assisted transport reaction.[19,20] NaP$_7$, a 2 eV-semiconductor material, plays a crucial role in the sodification and desodification processes in sodium ion batteries.[18] SnIP represents the first inorganic atomic-scale-double helix compound and (CuI)$_3$P$_{12}$ is an adduct phase from CuI and a neutral phosphorus chain.[21–23]

TiO$_2$ nanotubes are hollow nano-sized cylinders that form in vertically oriented arrays over large areas on the underlying substrate. The nanotubes are fabricated by electrochemical anodization of Ti films or foil in electrolytes typically containing F$^-$ through the simultaneous occurrence of field-assisted Ti oxidation, field-assisted dissolution of Ti and TiO$_2$, and chemical dissolution of TiO$_2$.[24,25] The as-synthesized nanotubes are amorphous and are crystallized to n-type semiconducting anatase either by annealing in air at temperatures of 350–550 °C or by a hydrothermal treatment at lower temperatures.[26,27] TiO$_2$

[a]Department of Chemistry, Technical University of Munich, Lichtenbergstr. 4, 85748 Garching, Germany. E-mail: tom.nilges@lrz.tum.de

[b]Department of Electrical and Computer Engineering, 9211-116 Street NW, Edmonton, Alberta, Canada T6G 1H9. E-mail: kshankar@ualberta.ca

† Electronic supplementary information (ESI) available. See DOI: 10.1039/c9na00084d

‡ Contributed equally.

nanotubes exhibit remarkable versatility in the type of substrate they can be grown on, having been demonstrated on Si, ITO-coated glass, FTO-coated glass, quartz, polyimide and Ti foil, and also as free-standing membranes.[28–30] Likewise, the nanotube diameter can be varied over a wide range (10 to 900 nm).[31,32] These characteristics make TiO_2 nanotubes ideal for the templated growth of inorganic phosphorus-based semiconductors through diffusive chemical vapor transport into the nanotube pores at elevated temperatures.

While electrodeposition and chemical vapor deposition into nanoporous anodic aluminium oxide (AAO) templates have been previously used to form nanorods and nanofibers of CdS, CdSe, Si, Bi, etc. exhibiting quantum confinement effects,[33–36] the application spectrum for semiconductor nanowires formed by chemical vapor transport deposition into anodic TiO_2 nanotube arrays is much greater. This is because the TiO_2 nanotubes are n-type semiconductors (charge carrier density $\sim 10^{18}$ to 10^{19} cm^{-3})[37] and allow the formation-in-place of a semiconductor heterojunction while AAO is an insulator, precluding the formation of a useful heterojunction. Furthermore, for a heterojunction to be electronically useful in applications that rely on light harvesting (photodetectors, photovoltaics, photocatalysts, and photoelectrochemical sensors) it is essential for excess carriers to be efficiently separated and for photons to be completely harvested. In this regard, vertically oriented nanotubes and nanowires are uniquely suited because the processes of charge separation and light absorption are orthogonalized.[38] Charge carriers created in a semiconductor nanorod formed inside the nanotubes need to merely travel a distance equal to the nanotube radius before encountering a heterojunction interface for charge separation while the high aspect ratio of the nanotubes ensures that even weakly absorbed photons are harvested. Furthermore, light trapping effects such as photonic crystals and resonant Mie scattering can be easily incorporated into the nanotubes to increase their photonic strength.[32,39] Indeed, heterojunctions of TiO_2 nanotubes with solution-processed semiconductors such as CdS, CdSe, PbS, Fe_2O_3, Cu_2-$ZnSnS_4$, g-C_3N_4, halide perovskites, etc. have been used to demonstrate efficient Z-scheme CO_2 reduction photocatalysts,[40] high performance water photolyzers,[41] selective gas sensors,[42] and high efficiency solar cells.[43,44] Herein, we introduce TiO_2–polyphosphide heterojunctions consisting of polyphosphide nanofibers formed by the hitherto unexplored process of chemical vapor transport into TiO_2 nanotube array templates.

2.   Results and discussion

Section 2.1 describes the synthesis of the TiO_2 nanotubes and nanohybrids in brief. Sections 2.2 and 2.3 describe our characterization of NaP$_7$@TiO$_2$ and SnIP@TiO$_2$ heterostructures. Following the same principle as that for NaP$_7$ and SnIP, the synthesis, characterization and physical property measurement details of $(CuI)_3P_{12}$ on TiO_2 heterostructures are circumstantiated, as well as a full description of all synthesis parameters and characterization techniques in the ESI Section.† Section 2.4 and 2.5 summarize X-ray Photoelectron Spectroscopy (XPS) and UV-Vis studies of the heterostructures, with details given in the ESI†

respectively. Section 2.6 deals with photocatalytic activity measurements and related characterization. Detailed interface photon-to-current efficiency performance as well as semiconductor–electrolyte interface analysis are described in the ESI† as well as sections on Electrochemical Impedance Spectroscopy (EIS), impedance-potential measurements, and Kelvin Probe Force Microscopy (KPFM).

2.1   Synthesis of polyphosphide@TiO$_2$ nanotube hybrids

A low-cost and easily accessible method to fabricate nanostructured photochemically active hybrid polyphosphide@TiO$_2$ heterostructures has been developed following a short-way transport reaction onto and into electrochemically fabricated TiO_2 nanotube membranes (Fig. 1). Synthesis details are given in the ESI.†

2.2   NaP$_x$@TiO$_2$ nanotubes

Fig. 2a displays the crystal structure of NaP$_7$ and a representative membrane after the gas phase deposition reaction is shown. Small crystals of NaP$_7$ were formed on the surface of the TiO_2 membrane (see Fig. 2b). A Scanning Electron Microscopy (SEM) image of the TiO_2 membrane cross section substantiates the growth of NaP$_7$ on both sides of the membrane. It is obvious from Fig. 2c that the crystal sizes are different on both sides which directly correlates with the TiO_2 nanotube pore width on either side. The cross-sectional images were taken after cutting the polyphosphides@TiO$_2$ nanotubes with a razor, taking the images along the cut edges. Obviously, the growth of the polyphosphide crystals started from the surface or even from inside the TiO_2 nanotube directly into the gas phase (see Fig. 3). Therefore, many crystals are grown straight out of the nanotubes. A second hint for a growth from the inside into the gas phase might be the differences in the sizes of the crystals on both sides of the membrane (corresponding SEM data in Table S1†). On the other hand, the size of the TiO_2 nanotubes can directly define the diameter of the resulting NaP$_x$ crystals ($x = 7$, 15).

Two visually different main fractions lying on the top and bottom of the TiO_2 membrane sides were observed. The
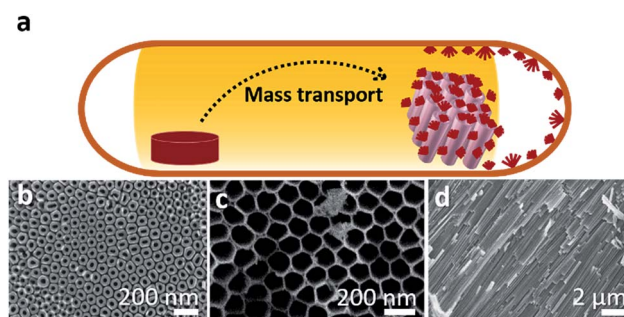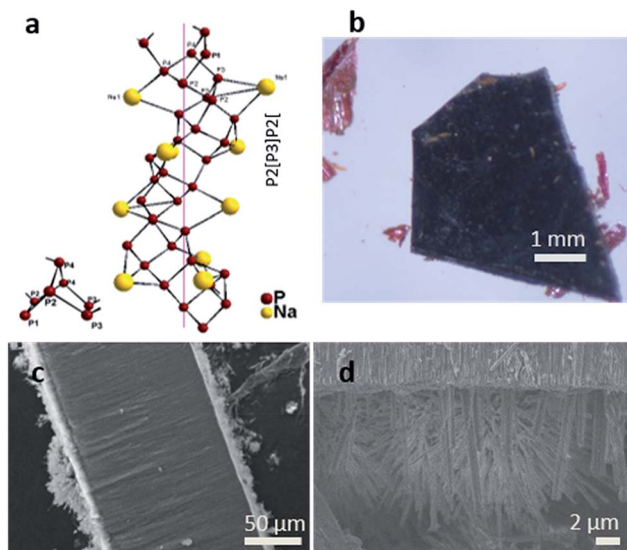

Fig. 1 (a) Starting materials (red pellet) are transported onto and into TiO_2 nanotube membranes (brown) via a gas phase. (b) Representative SEM pictures of the electrochemically prepared TiO_2 nanotube membranes used in a mineralizer-driven short-way transport reaction in the bottom side view, (c) top side view, and (d) side view.

Fig. 2 (a) Structure with a representative Na-coordinated polyphosphide substructure of NaP$_7$. (b) A TiO$_2$ nanotube membrane reacted with Na and P *via* a gas phase. (c) SEM images show the cross section of a membrane. (d) Intact TiO$_2$ nanotubes of the membrane shown in (b) and NaP$_7$ crystals grown on top of the membrane surface. Many crystals have grown straight out of the nanotubes.
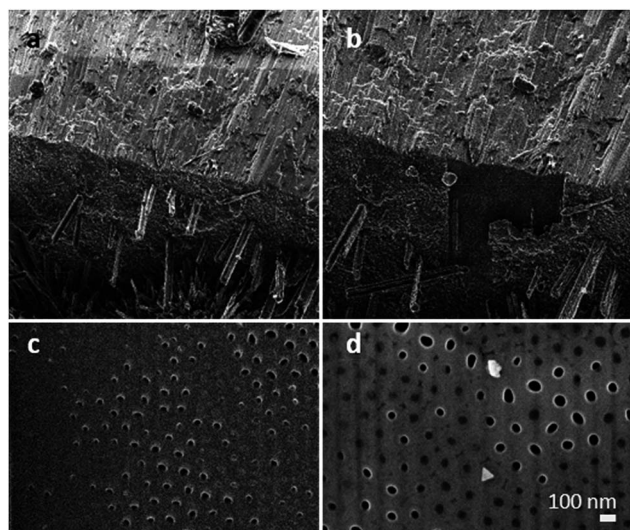

Fig. 3 FIB measurement on a NaP$_x$@TiO$_2$ nanotube membrane. FIB-SEM image (a) before and (b) after FIB-milling of the TiO$_2$ membrane surface area. (c) FIB-SEM and (d) SEM image of the milled area. Filled tubes show a lighter grey contrast than the non-filled appearing holes. An approx. 1 : 1 ratio was ascertained.

samples were manually separated, and data collection of powder X-ray diffraction led to a nearly phase pure pattern of NaP$_7$ (main fraction) and a diffraction pattern of NaP$_{15}$ (minor fraction) reflecting distinct texture effects (see S1a and b). To verify the assumption that a significant transport of the material occurred *via* the gas phase to the inside of the nanotubes, we examined the cross section of a broken membrane by position-sensitive EDS scans (Table S1†). The data along the cross section

of the membrane show a constant Na : P ratio of approx. 1 : 9 towards the top side view of the membranes (larger holes), where the crystals on the surface show a larger size and a ratio of 1 : 4 towards the bottom side of the membranes (smaller holes), where the crystals show a smaller size. This finding substantiates our hypothesis that Na and P were transported into the TiO$_2$ nanotubes along a certain length of the membrane. To verify the filling grade of the nanotubes, and therefore the efficiency of the gas phase transport, a FIB experiment was performed on a selected spot of the membrane. The FIB was used to cut off the upper part down to 15 nm of the membrane to facilitate an observation of the nanotube's subsurface. We found non-filled and filled tubes on the area we treated (see Fig. 3). Taking a closer look at the tubes, a filling grade of 50% can be estimated from the FIB pictures.

To determine the filling elemental depth profile, the FIB milled area (shown in Fig. 4) was analysed *via* Auger electron spectroscopy (AES) and microscopy (see Fig. 4 and AES spectra in Fig. S2†). Fig. 4a shows locally analysed FIB-milled spots with spot 1 demonstrating the analysis of a tube considered empty; notably, it is the only spot indicating the presence of carbon. Due to sample cleaning by argon ion bombardment, it is assumed that carbon has been cleaned off, as it is not present in all other spots but spot 1 being inaccessible to cleaning and therefore showing the presence of C. Spots 2–6 have much higher P contents than spot 1 even after deducting the C content (a proportionate rise of P to 18.9 at%). This suggests that the spot 2–6 nanotubes were filled, while the spot 1 tube was not; the signal at spot 1 of P is not attributed to the P content in the apparently empty nanotube but appears due to the approximately 10 nm resolution of the instrument. The most prominent Na peaks appear at 24 eV (Na KLL, overlap in AES spectra, Fig. S2†) and taking the relatively low Na to P ratio into account, a merely weak peak at 979 eV (Na LVV).

Raman spectroscopy on the surface and cross section of a membrane (cut apart with a razor) was carried out to validate the successful transport of the material into the TiO$_2$ nanotube membranes. We measured the depth of intake of a material by moving the Raman laser gradually along the cross section, acquiring spectra at specific spots. The laser has a standard mode spot size of 1.5 microns (at 50× magnification). From
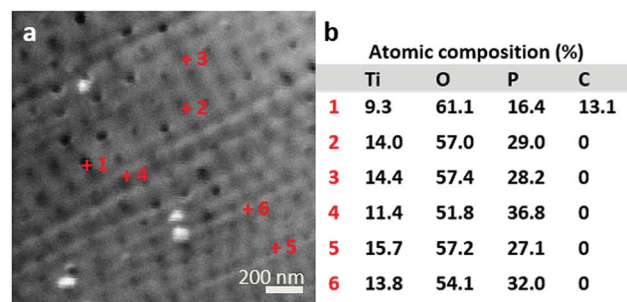
Fig. 4 (a) Measured spots of Auger electron spectroscopy of the FIB milled NaP$_x$@TiO$_2$ nanotube specimen. (b) Detected atomic composition. Each measured composition has an error of approximately 10% of the value reported.

	Ti	O	P	C
1	9.3	61.1	16.4	13.1
2	14.0	57.0	29.0	0
3	14.4	57.4	28.2	0
4	11.4	51.8	36.8	0
5	15.7	57.2	27.1	0
6	13.8	54.1	32.0	0

a series of spectra recorded at different depths and from both sides of the membrane, we found the penetration of NaP_x through the whole membrane. Raman spectra recorded along the cross section at several distances from the surface suggest two additional phases next to TiO_2 anatase after gas phase synthesis together with the nanotube membranes. The most prominent modes at 352 cm^{-1} (NaP_7) and 377 cm^{-1} (NaP_{15}) of the Raman data show the simultaneous presence of NaP_7 at 9 µm and NaP_{15} at 13 µm distance from the bottom side of the membrane surface next to a signal at 145 cm^{-1} for TiO_2 anatase (E_g) (Fig. 5). By recording along the tube length characteristic signals of less intensity confirm the presence in the centre of the nanotubes up to the top membrane side, where NaP_{15} can be found at 11 and 14 µm deep into the surface. Obviously, the crystallinity was significantly reduced going deeper into the membrane.

Representative single TiO_2 nanotubes were separated from a membrane by an ultrasonication step and STEM imaging and EDS mapping was performed to corroborate the filling of the tubes with NaP_x, as shown in Fig. 6. Na and P were detected along the full tube length. CuI was used as a transport agent and can be displayed in the elemental analysis in significant amounts. Cu was only present in defined crystals attached to the membranes and it could not be detected in reasonable amounts inside the tubes. Such defined crystals are possibly formed during the transport process as side phases or represent the remaining transport agent.

The chemical vapor deposition of NaP_7 and NaP_{15} phases onto TiO_2 nanotube membranes can be verified *via* powder XRD patterns. As SEM-EDS data show, the nanotubes are filled from both sides with NaP_x phases. This can be further proved by EDS-
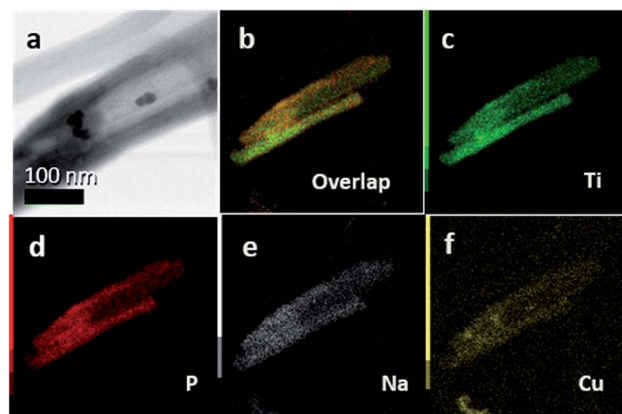

Fig. 6 (a) STEM bright-field image of TiO_2 nanotubes separated from a membrane by an ultrasonication procedure. (b) STEM-EDS shows overlaid elemental mapping of the elements Ti, P, Na and Cu. (c) Ti (representing TiO_2) nanotubes with (d) P, continuously distributed along the tubes and (e) Na substantiating the filling of the full nanotube length. (f) Cu from the mineralizer is only present in small amounts.

and Auger-results after FIB-milling into a depth of about 200 nm of the membranes. Raman spectra recorded at the center of the membrane cross section after synthesis show signals in the ranges of NaP_7 and NaP_{15} modes next to the anatase phase. After an ultrasonication process, Scanning Transmission Electron Microscopy-Energy-dispersive X-ray Spectroscopy (STEM-EDS) measurements show furthermore the presence of Na, P and Cu of the transport agent within the single tubes.

2.3 SnIP@TiO$_2$ nanotubes

We have further substantiated the chemical vapor deposition of the inorganic double helical semiconductor SnIP featuring a band gap of 1.86 eV on TiO_2 nanotube arrays (see Fig. 7a).[17] SnIP is anticipated to be formed from the gaseous phases of the
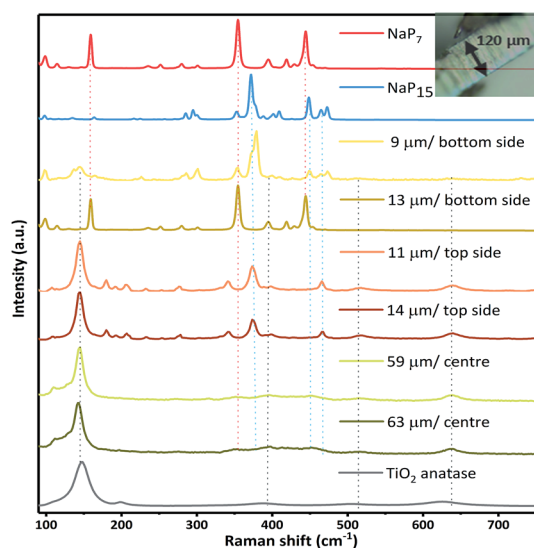

Fig. 5 Raman spectroscopy of NaP_x@TiO_2 membranes. From top to bottom: reference Raman spectrum of NaP_7 (red) and NaP_{15} (blue), and spectra of a NaP_x@TiO_2 membrane cross section measured at approx. 9 and 13 µm distance from the surface (membrane bottom side), at approx. 11 and 14 µm distance from the surface (membrane top side), at approx. 59 and 63 µm (membrane centre) and a fresh TiO_2 membrane (anatase, grey).

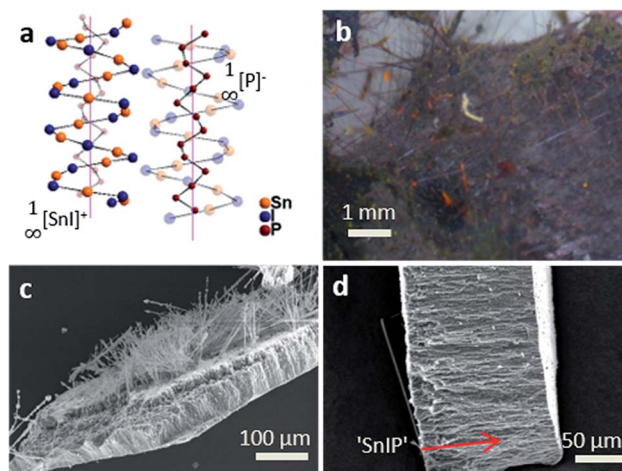Fig. 7 (a) Structure of SnIP with two representative strands. (b) A TiO_2 nanotube membrane reacted with SnIP *via* a gas phase. (c) Cross section and surface of SnIP@TiO_2 nanotube membranes. (d) EDS of the cross section showing SnIP along the nanotubes.

precursors and a comproportionation reaction of Sn and SnI_4 to SnI_2. Therefore, no additional mineralizer was needed to cover the surface of the TiO_2 nanotube membranes with SnIP as depicted in the microscopy images in Fig. 7b and c. The SEM image substantiates the growth of SnIP on the nanotube, when detecting the elemental composition via EDS measurements. The detection of Sn and I was diminished going further into the tubes (Table S2†). A possible explanation is that during the transport reaction through a gas phase the formation of pure phosphorus species deeper in the nanotubes can be more likely than the double helical structure of $\frac{1}{\infty}[SnI^+]$– and $\frac{1}{\infty}[P^-]$–chains. Powder X-ray diffraction verifies the formation of crystalline SnIP on the TiO_2 membranes (Fig. S3†).

STEM imaging after the separation of the TiO_2 nanotubes by an ultrasonication process shows a set of nanotubes with a size of ~80–100 nm per tube. Elemental mapping confirms Ti (representing TiO_2), P, Sn, and I with a distribution of P along the tube length. Sn and I appear to be present in smaller amounts in a TiO_2 tube (Fig. 8).

SnIP was grown successfully onto and into TiO_2 nanotube arrays via a gas phase as verified using powder X-ray diffraction and SEM-EDS. The transportation of the ternary compounds into the nanotubes was demonstrated with STEM-EDS analysis.

2.4 XPS studies

We performed XPS studies on the pure semiconductors NaP_x, SnIP and $(CuI)_3P_{12}$ and the three semiconductor@TiO_2 nanotube heterostructures in order to verify the surface compositions, binding energies and oxidation states of the materials (Fig. S7–S9 and Table S6†). All oxidation states in the heterostructure systems are consistent with the ones observed for the pure compounds along with surface oxidized phosphates (P_xO_y). In the case of (NaP_7, NaP_{15})@TiO_2 we found a shift of the Na1s peak in NaP_7@TiO_2 to higher binding energy which might be due to partial charge transfer from NaP_7 to the surface of TiO_2 and doping of the TiO_2 surface with Na^+ ions to some extent. The peak positions of Ti and O remained unchanged

upon semiconductor loading into the tubes (Fig. S7†). A comparable charge transfer behaviour was observed for the $(CuI)_3P_{12}$@TiO_2 heterostructure compound (see Fig. S8†).

XPS spectra of SnIP@TiO_2 do not show any significant change of the Sn, I and P peaks which we interpret as the absence of significant bonding interaction between the two phases (shown in Fig. S9†).

2.5 UV-Vis spectra

The absorption properties of materials in the UV-Vis region were determined by diffuse reflectance UV-Vis spectroscopy (Fig. S6a†). The absorption spectra of TiO_2 nanotubes show an intense band at 330 nm with band tailing up to 384 nm, which corresponds to a valence band to conduction band (O2p → Ti3d) transition.[45,46] The UV-Vis spectra of NaP_7 displayed broad absorption in the visible region extended up to 800 nm, which is attributed to charge generation in the phosphide chain motif. The NaP_7@TiO_2 heterostructures displayed an absorption band which corresponded to TiO_2 along with an absorption profile in the visible region due to the presence of NaP_7. Pristine SnIP displayed a broad absorption edge up to 700 nm which is shifted up to 500 nm in SnIP@TiO_2, with a slight increase in the absorption profile at higher wavelengths (Fig. S10†). The UV-Vis spectra of pristine $(CuI)_3P_{12}$ show an intense absorption edge extended up to 440 nm which is slightly decreased in $(CuI)_3$-P_{12}@TiO_2 samples (Fig. S10†). To probe the visible light absorption of the samples, the optical band gap of each material was determined using a Tauc plot by plotting a graph of $(\alpha h\nu)^{1/2}$ vs. $h\nu$ followed by extrapolation of a linear tangent to the abscissa, where α is the absorption coefficient, h is the Planck constant, and ν is the light frequency (Fig. S10†). The band gaps for TiO_2, NaP_7, NaP_7@TiO_2, SnIP, SnIP@TiO_2, $(CuI)_3P_{12}$ and $(CuI)_3P_{12}$@TiO_2 (see Table 1) are in close agreement with reported values. Due to the band gap values a certain absorption in the visible light region is present (Fig. S6†).

2.6 Photocatalytic activity measurement

The photocatalytic performance of the hybrid materials was discerned by photoelectrochemical water splitting experiments. A three-electrode configuration was used, composed of pristine/hybrid materials deposited on FTO glass as the photoanode, Pt as the cathode and Ag/AgCl as the reference electrode, all immersed in a 0.1 M KOH electrolyte. The photoanode was irradiated with AM1.5 G solar simulated light having a power density of 100 mW cm^{-2} on the surface of the sample. The photocurrent density per cm^2 was measured in linear sweep voltammetry (LSV) mode by switching the applied bias from −1.0 V to +0.8 V vs. Ag/AgCl. The dark current was also measured to compare the photoelectrochemical response. At an applied bias of 0.6 V vs. Ag/AgCl (1.23 V vs. RHE which is the water oxidation potential), the photocurrent density values of TiO_2, NaP_7, NaP_7@TiO_2, SnIP, SnIP@TiO_2, $(CuI)_3P_{12}$ and $(CuI)_3P_{12}$@TiO_2 are shown in Table 1. Under dark conditions the current density remains almost zero, while after irradiation under solar simulated light bare TiO_2 shows extremely low photocurrent (0.21 mA cm^{-2}) which is in good agreement with
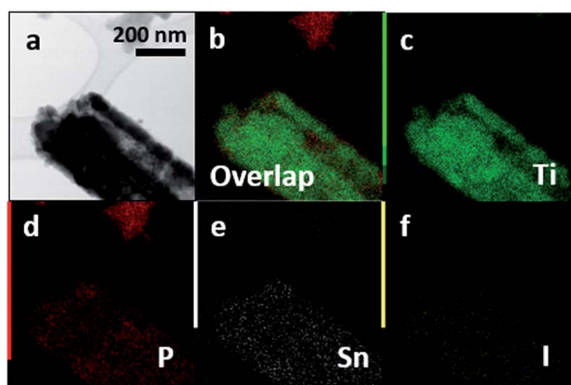

Fig. 8 (a) STEM bright-field image of TiO_2 nanotubes separated from a membrane by an ultrasonication procedure. (b) Elemental mapping of overlaid elements Ti (representing TiO_2), P, Sn and I. (c) Ti and (d) P substantiating P distributed along the length of TiO_2 nanotubes with (e) Sn and (f) I in small amounts.

Table 1 Energies of band gaps, values of photocurrent density, maximum ABPE, IPCE, and APCE in % of TiO_2 nanotubes, NaP_7, $NaP_7@TiO_2$, SnIP, SnIP@TiO_2, $(CuI)_3P_{12}$ and $(CuI)_3P_{12}@TiO_2$ obtained by UV–Vis, linear sweep voltammetry and corresponding calculations

| Sample	Band gap [eV]	Photocurrent density [mA cm^{-2}]	Max ABPE [%]	IPCE [%]	APCE [%]
TiO_2	3.05	0.21	0.07	0.007	0.01
NaP_7	1.28	0.20	0.04	0.04	0.06
$NaP_7@TiO_2$	1.87	0.22	0.05	0.36	0.43
SnIP	1.84	0.20	0.02	2.0	0.46
SnIP@TiO_2	2.22	0.84	0.20	0.20	3.2
$(CuI)_3P_{12}$	2.84	0.41	0.06	0.46	0.78
$(CuI)_3P_{12}@TiO_2$	2.73	0.43	0.09	0.48	1.19

its large band gap ($\sim$3.2 eV), as shown in Fig. 9a. Similarly, the photocurrent density for bare NaP_7, $(CuI)_3P_{12}$ and SnIP remained low due to the inability of poorly oxidative holes to facilitate water splitting. Thus, the order of performance is SnIP > $(CuI)_3P_{12}$ > NaP_7. Furthermore, the hybrids $NaP_7@TiO_2$ and $(CuI)_3P_{12}@TiO_2$ also displayed a small improvement in photocatalytic performance over the pristine phosphide material which might be due to unfavourable Fermi level alignment resulting in sluggish charge separation. However, hybrids of

SnIP phosphides with TiO_2 (SnIP@TiO_2) demonstrated a much higher photocurrent density (0.82 mA cm^{-2}) than individual components and $NaP_7@TiO_2$ and $(CuI)_3P_{12}@TiO_2$; this suggests the formation of a heterojunction and feasible transfer of electrons and holes. The higher photocurrent for SnIP@TiO_2 is attributed to better coverage of the TiO_2 surface by SnIP and more long-range ordering of the SnIP helix which facilitates faster charge injection into the conduction band of TiO_2. To validate the photoresponse of materials, the photocurrent was measured during a light on–off cycle, which clearly demonstrated the materials' photo-responsive nature (Fig. S11†). Furthermore, the ability to drive water splitting at longer wavelengths was proved by measuring the photocurrent response of the materials under 425 nm and 505 nm wavelength light irradiation having a power density of 54.15 and 40.48 mW cm^{-2}, respectively, at the surface of the samples (Fig. 9b). Again, the highest photocurrent density (0.32 mA cm^{-2} at 450 nm and 0.34 mA cm^{-2} at 505 nm) was obtained for the SnIP@TiO_2 composite (Fig. 9b). Furthermore, on–off experiments clearly confirmed the higher wavelength response of the SnIP@TiO_2 composite (Fig. S12†).

To quantify the material system/interface performance, the following diagnostic efficiencies were measured according to derivations given in the ESI.† The maximum applied bias photon-to-current efficiency percentage (ABPE%) for TiO_2, NaP_7, $NaP_7@TiO_2$, SnIP, SnIP@TiO_2, $(CuI)_3P_{12}$ and $(CuI)_3$-$P_{12}@TiO_2$ was calculated and is listed in Table 1 (Fig. 9c). SnIP@TiO_2 nanohybrids show the highest performance (3.2%) which was much higher than that of the other hybrids. Furthermore, the ABPE% of SnIP@TiO_2 was 10 times higher than that of pristine SnIP which demonstrates that hybrid material formation with TiO_2 increased photocatalytic performance significantly.

The incident photon-to-current efficiency percentage (IPCE%) and absorbed photon-to-current efficiency percentage (APCE%) for TiO_2, NaP_7, $NaP_7@TiO_2$, SnIP, SnIP@TiO_2, $(CuI)_3P_{12}$ and $(CuI)_3P_{12}@TiO_2$, listed in Table 1, demonstrate that heterostructure formation overall improves the photocatalytic performance of materials in the visible regime.

To gain insight into the charge transfer mechanisms in the materials and determine the band structure of the materials, work function spectra and valence band spectra were recorded using ultraviolet photoelectron spectroscopy (UPS). The work
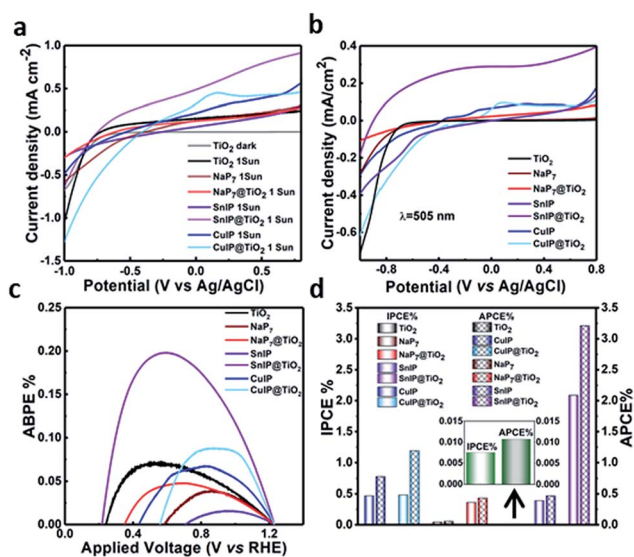
Fig. 9 (a) Linear sweep voltammogram of TiO_2 under dark conditions and under 1 solar simulated AM1.5 G light irradiation (100 mW cm^{-2}) for bare TiO_2 nanotubes, NaP_7, $NaP_7@TiO_2$, SnIP, SnIP@TiO_2, $(CuI)_3P_{12}$, and $(CuI)_3P_{12}@TiO_2$. (b) Photocurrent density vs. applied voltage plot under 505 nm LED light irradiation (40.5 mW cm^{-2}) of TiO_2 nanotubes, NaP_7, $NaP_7@TiO_2$, SnIP, SnIP@TiO_2, $(CuI)_3P_{12}$, and $(CuI)_3P_{12}@TiO_2$. (c) ABPE% vs. RHE plot under AM1.5 G light irradiation (100 mW cm^{-2}) for TiO_2 nanotubes, NaP_7, $NaP_7@TiO_2$, SnIP, SnIP@TiO_2, $(CuI)_3P_{12}$, and $(CuI)_3P_{12}@TiO_2$. (d) IPCE% under 505 nm LED light irradiation (40.5 mW cm^{-2}) for TiO_2, NaP_7, $NaP_7@TiO_2$, SnIP, SnIP@TiO_2, $(CuI)_3P_{12}$, and $(CuI)_3P_{12}@TiO_2$ and APCE% under 505 nm LED light irradiation (40.5 mW cm^{-2}) for TiO_2 nanotubes, $(CuI)_3P_{12}$, $(CuI)_3P_{12}@TiO_2$, NaP_7, $NaP_7@TiO_2$, SnIP, and SnIP@TiO_2. Color: TiO_2 under dark conditions (black), TiO_2 and under AM1.5 G light irradiation TiO_2 nanotubes (grey), NaP_7 (brown), $NaP_7@TiO_2$ (red), SnIP (violet), SnIP@TiO_2 (pink), $(CuI)_3P_{12}$ (deep blue), and $(CuI)_3P_{12}@TiO_2$ (light blue) (CuIP $\Rightarrow$ $(CuI)_{12}P_3$).

function was calculated using the expression WF (ϕ) = 21.21 − $E_{\text{cut-off}}$, where 21.21 eV is the energy of the incident He(I) line of a He discharge lamp, and $E_{\text{cut-off}}$ is the cut-off energy of secondary electrons. The point of intersection after extrapolation of the linear regions of the graphs results in the cut-off energy values. From the graph, the cut-off energy and value of work function for TiO$_2$, NaP$_7$, NaP$_7$@TiO$_2$, (CuI)$_3$P$_{12}$, (CuI)$_3$-P$_{12}$@TiO$_2$, SnIP and SnIP@TiO$_2$ are listed in Table 2 (Fig. 10 and insets). It should be noted that unexpectedly, we observe that the WF of the NaP$_7$@TiO$_2$ and SnIP@TiO$_2$ hybrids falls above and below that of the pristine materials, respectively. This may be due to small amounts of metal-ion surface doping in the hybrids, where Na$^+$ decreases the charge density on TiO$_2$ and Sn^{2+} increases the charge density on TiO$_2$; on the other hand, Cu$^+$ is a closed-shell d-block element with a similar charge distribution to Ti^{4+}, which may explain why this effect does not seem to be observed as strongly in this case. Furthermore, based on the P 2p region in NaP$_7$, a higher degree of oxidation seems to occur in the pristine material compared to its hybrid here, changing the charge distribution on the phosphide backbone, and shifting the WF. The position of valence band maxima (VB$_{\text{max}}$) obtained from UPS valence band spectra of NaP$_7$, NaP$_7$@TiO$_2$, (CuI)$_3$P$_{12}$, (CuI)$_3$P$_{12}$@TiO$_2$, SnIP and SnIP@TiO$_2$ is also shown in Table 2 (Fig. 10, inset). Furthermore, the valence band position of bare TiO$_2$ nanotubes determined from XPS valence band spectra was found to be 3.15 eV below the Fermi level (Fig. S9†).

On the basis of the obtained band structure and band gap, we have proposed a plausible mechanism of improved photocatalytic performance of polyphosphide@TiO$_2$ materials (Fig. 10). In general, to achieve efficient water splitting the conduction band position of the semiconductor should be more negative than 0.00 V vs. NHE at pH-0 (reduction potential of protons, H$^+$/H$_2$) and overpotential, while the valence band position should be more positive than +1.23 V vs. NHE at pH-0 (oxidation potential of water, H$_2$O/O$_2$). So, the band gap of the materials should be wider than 1.23 eV. TiO$_2$ has a wide band gap of approximately 3.2 eV with appropriate band positions (conduction band, E_{CB}; −0.26 V and valence band, E_{VB}; +2.94 V vs. NHE at pH 0) to drive the water splitting reaction; however, its large band gap means the photocatalytic response of TiO$_2$ remains too low under visible irradiation. On the other hand, inorganic phosphides (NaP$_7$, (CuI)$_3$P$_{12}$ and SnIP) absorb
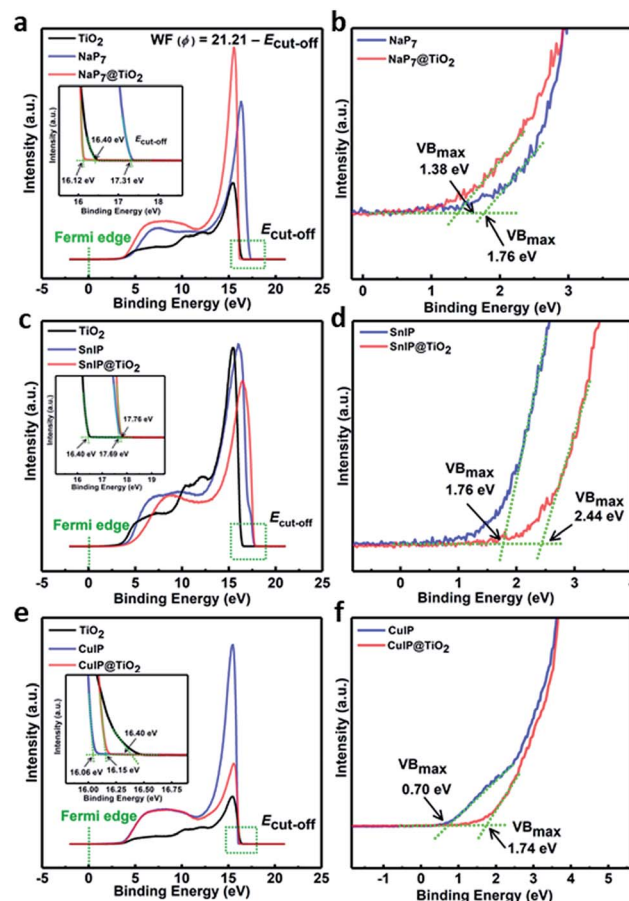

Fig. 10 UPS work function spectra and inset showing the cut-off energy ($E_{\text{cut-off}}$) of (a) TiO$_2$ nanotube membranes, NaP$_7$ and NaP$_7$@-TiO$_2$, (c) TiO$_2$ nanotube membranes, SnIP and SnIP@TiO$_2$, and (e) TiO$_2$ nanotube membranes, (CuI)$_3$P$_{12}$ and (CuI)$_3$P$_{12}$@TiO$_2$. The value of work function (WF) was determined from the UPS work function spectra by using the equation WF (ϕ) = 21.21 − $E_{\text{cut-off}}$, where 21.21 eV is the energy of the incident He(I) line of a He discharge lamp used for UPS. UPS valence band spectra showing valence band maxima below the Fermi level of (b) NaP$_7$ and NaP$_7$@TiO$_2$, (d) SnIP and SnIP@TiO$_2$ and (f) (CuI)$_3$P$_{12}$ and (CuI)$_3$P$_{12}$@TiO$_2$ (CuIP ⇒ (CuI)$_{12}$P$_3$).

well in the UV-Vis region to generate electron–hole pairs due to their low band gap (1.28, 2.84 and 1.86 eV) (Fig. S6†). From the Mott–Schottky measurements, the flat band potential values for NaP$_7$, (CuI)$_3$P$_{12}$ and SnIP were found to be −0.670, −0.721 and −0.730 V, respectively, vs. Ag/AgCl, which might be considered the position of the conduction band, E_{CB} (Table 2). As the band position is usually expressed on the NHE scale in water splitting, the conduction band position of NaP$_7$, (CuI)$_3$P$_{12}$ and SnIP was calculated to be −0.471, −0.522 and −0.531 V, respectively, vs. NHE at pH 0. By taking the band gap and conduction band position into account, the estimated valence band position for NaP$_7$, (CuI)$_3$P$_{12}$ and SnIP was found to be +0.809, +2.318 and +1.309 V, respectively, vs. NHE at pH 0. These values indicate that the valence band positions of NaP$_7$ and SnIP are not positive enough to afford water oxidation, while the valence band position of (CuI)$_3$P$_{12}$ was slightly more positive than the water oxidation potential and thus generates poorly oxidizing

Table 2 Secondary electron cut-off energies ($E_{\text{cut-off}}$), values of work function (WF) and valence band maxima (VB$_{\text{max}}$) obtained from UPS measurements of TiO$_2$ nanotubes, NaP$_7$, NaP$_7$@TiO$_2$, SnIP, SnIP@TiO$_2$, (CuI)$_3$P$_{12}$ and (CuI)$_3$P$_{12}$@TiO$_2$

Sample	$E_{\text{cut-off}}$ [eV]	WF [eV]	VB$_{\text{max}}$
TiO$_2$	16.40	4.81	3.15
NaP$_7$	17.31	3.90	1.76
NaP$_7$@TiO$_2$	16.12	5.09	1.38
SnIP	17.69	3.52	1.76
SnIP@TiO$_2$	17.76	3.45	2.44
(CuI)$_3$P$_{12}$	16.06	5.15	0.70
(CuI)$_3$P$_{12}$@TiO$_2$	16.15	5.06	1.74

holes. This explains the observed negligibly small photocurrent for pristine NaP_7 and SnIP, and the slightly improved photocurrent for $(CuI)_3P_{12}$. After hybrid material formation, the photocatalytic performance of $NaP_7@TiO_2$, $(CuI)_3P_{12}@TiO_2$ and $SnIP@TiO_2$ was improved (Fig. 9d). However, $SnIP@TiO_2$ displayed a much greater rise in photocurrent compared to the other hybrid nanostructures. The improved photocurrent response can possibly be explained based on the Fermi level alignment between heterojunctions, charge carrier concentration, flat band potential and position of the valence band. This feature has been observed for fibrous red phosphorus@TiO_2 and black phosphorus@TiO_2 hybrids.[47] A drastic improvement of the photocatalytic activity was also reported for $SnIP@C_3N_4$ heterostructures where an ideal contact between the two materials is realized by a self-assembly process.[48] Additional experiments are planned to substantiate this assumption for the titular compounds. Mott–Schottky analysis shows a shift in the flat band potential from -0.471 and -0.522 V vs. NHE in pristine NaP_7 and $(CuI)_3P_{12}$ to -0.581 and -0.493 V vs. NHE in $NaP_7@TiO_2$ and $(CuI)_3P_{12}@TiO_2$ which implies a possible Fermi level alignment (flow of electrons from one semiconductor to another for equilibrating the Fermi level position), and the conduction band shifted slightly due to downward band bending in NaP_7 and $(CuI)_3P_{12}$ and upward band bending in TiO_2, respectively, (see Fig. S17 in the ESI†). Interestingly, the conduction band position (E_{CB}) of SnIP (-0.531 V) was shifted drastically toward a more negative potential in $SnIP@TiO_2$ (-1.731 V), which reveals more prominent band bending. The higher band bending and more negative conduction band position in $SnIP@TiO_2$ lead to more efficient charge separation, which facilitated superior water splitting.

From the UPS VB spectra, the VB_{max} position of $SnIP@TiO_2$ was found to be deeper than that of $NaP_7@TiO_2$ and $(CuI)_3P_{12}@TiO_2$ which suggests the generation of more oxidative holes in the $SnIP@TiO_2$ heterostructure to drive water splitting (Fig. 10). Additionally, the depletion width for $SnIP@TiO_2$ was found to be 922.89 nm which demonstrates an effective inbuilt electrical field in the space charge region; this value was much higher than that of $NaP_7@TiO_2$ (118.95 nm) and $(CuI)_3P_{12}@TiO_2$ (157.14 nm), and clearly supports better charge transfer in $SnIP@TiO_2$ (Table 2). Furthermore, the recombination lifetime of photoexcited species plays an important role in photocatalysis and a long lifetime is expected for better photocatalytic performance. The longer recombination lifetime of $SnIP@TiO_2$ (2.40 μs) in comparison to $NaP_7@TiO_2$ (1.90 μs) and $(CuI)_3P_{12}@TiO_2$ (1.90 μs) signifies the availability of more electrons and holes to drive hydrogen evolution and water oxidation reactions (Table 2). The morphological and surface coverage might be responsible for the higher performance of the $SnIP@TiO_2$ nanostructure. SnIP has a helical structure composed of an inner P helix $^1_\infty[P^-]$ chain and an outer helical $^1_\infty[SnI^+]$ helix winding together in long range ordering which generates a rod like structure. Due to long range ordering in 1D SnIP, better charge mobility can be achieved relative to short range NaP_7 and $(CuI)_3P_{12}$ resulting in better charge transfer to TiO_2. The occupancy of the nanotubes was also much higher in $NaP_7@TiO_2$ and $(CuI)_3P_{12}@TiO_2$ than $SnIP@TiO_2$, which might reduce the effective exposed surface area to light and electrolyte semiconductor interface contact leading to lower photocatalytic performance.

3. Conclusions

A gas-phase transport reaction was employed as an effective method to deposit complex binary and ternary polyphosphide compounds into TiO_2 nanotube arrays. The underlying short-way transport reaction by mineralization is a viable approach for the synthesis of hybrid materials. Three different substances, binary sodium polyphosphides, ternary SnIP, and $(CuI)_3P_{12}$, were successfully reacted with electrochemically fabricated TiO_2 nanotube membranes. The synthesized polyphosphides onto and into the TiO_2 nanotubes were analyzed with several spectroscopic and diffraction methods such as XRD, EDS-analysis, XPS, Auger electron and Raman spectroscopy and STEM analysis. SEM, HR-TEM, Auger electron spectroscopy, and elemental mapping of intact and cross sections of nanohybrids substantiated the successful deposition of materials inside the tube with excellent occupancy (a filling grade of ~50%).

STEM followed by EDS analysis proved the presence of the binary NaP_x phase as well as $(CuI)_3P_{12}$ along the full length of the TiO_2 nanotubes. STEM-EDS experiments of the ternary phase SnIP showed a higher distribution of P than Sn and I along TiO_2 nanotubes. Raman spectra recorded at the surface and along the razor-cut cross section of the nanotubes can verify the growth of NaP_x phases continuously along the nanotubes (120 μm in length) and $(CuI)_3P_{12}$ up to 22 μm into the nanotubes (63 μm in length). The herein reported hybrid materials displayed enhanced photoelectrochemical water splitting performance under visible light compared to individual components due to the possible formation of a heterojunction facilitating better charge separation. Considering the unusual values of the WF of $NaP_7@TiO_2$ and $SnIP@TiO_2$, further study of the interfaces may be warranted. Nevertheless, lower electronic bandgaps, negative conduction band positions of the composites, long recombination lifetime, better charge carrier mobility and deep valence band positions were responsible for improved visible light performance. This feature may lead to higher conversion efficiencies for optoelectronic applications such as in photodetectors, photovoltaics, photo-electrochemical catalysts and sensors. With a special focus on the mineralization concept, further heterostructures between 1D semiconductors and nanostructured materials are being prepared.

Authors contribution

E. Ü. and R. K. synthesized the polyphosphide hybrid materials and characterized them using Helium Microscopy, SEM, and STEM-EDS. P. Kumar performed XPS, UPS and photoelectrochemical studies and was involved in the interpretation of the obtained results. U. K. T. carried out the KPFM measurements. P. Kar was responsible for the electrochemical characterization. K. S. and T. N. supervised the research and edited the manuscript. All authors were involved in writing their respective parts.

Conflicts of interest

There are no conflicts to declare.

Abbreviations

CuIP	$(CuI)_3P_{12}$
SEM	Scanning electron microscopy
EDS	Energy dispersive X-ray spectroscopy
FIB	Focused ion beam
HR-TEM	High resolution transmission electron microscopy
XRD	X-ray diffraction
XPS	X-ray photoelectron spectroscopy
STEM	Scanning transmission electron microscopy
ITO	Indium-doped tin oxide
FTO	Fluorine-doped tin oxide
UV-Vis	Ultraviolet-visible spectroscopy
NHE	Normal hydrogen electrode

Acknowledgements

References

1 T. Hisatomi, J. Kubota and K. Domen, *Chem. Soc. Rev.*, 2014, **43**, 7520–7535.

2 P. Kalisman, Y. Nakibli and L. Amirav, *Nano Lett.*, 2016, **16**, 1776–1781.

3 K. Iwashina and A. Kudo, *J. Am. Chem. Soc.*, 2011, **133**, 13272–13275.

4 M. Higashi, K. Domen and R. Abe, *J. Am. Chem. Soc.*, 2012, **134**, 6968–6971.

5 J. Schneider, M. Matsuoka, M. Takeuchi, J. Zhang, Y. Horiuchi, M. Anpo and D. W. Bahnemann, *Chem. Rev.*, 2014, **114**, 9919–9986.

6 Y. Ma, X. Wang, Y. Jia, X. Chen, H. Han and C. Li, *Chem. Rev.*, 2014, **114**, 9987–10043.

7 J. Tang, J. R. Durrant and D. R. Klug, *J. Am. Chem. Soc.*, 2008, **130**, 13885–13891.

8 S. J. A. Moniz, S. A. Shevlin, D. J. Martin, Z.-X. Guo and J. Tang, *Energy Environ. Sci.*, 2015, **8**, 731–759.

9 K. Iwashina, A. Iwase, Y. H. Ng, R. Amal and A. Kudo, *J. Am. Chem. Soc.*, 2015, **137**, 604–607.

10 Z. Yu, F. Li and L. Sun, *Energy Environ. Sci.*, 2015, **8**, 760–775.

11 Y.-C. Pu, G. Wang, K.-D. Chang, Y. Ling, Y.-K. Lin, B. C. Fitzmorris, C.-M. Liu, X. Lu, Y. Tong, J. Z. Zhang, Y.-J. Hsu and Y. Li, *Nano Lett.*, 2013, **13**, 3817–3823.

12 M. Ge, Q. Li, C. Cao, J. Huang, S. Li, S. Zhang, Z. Chen, K. Zhang, S. S. Al-Deyab and Y. Lai, *Adv. Sci.*, 2017, **4**, 1600152.

13 R. Singh, R. Bapat, L. Qin, H. Feng and V. Polshettiwar, *ACS Catal.*, 2016, **6**, 2770–2784.

14 M. Bawohl and T. Nilges, *Z. Anorg. Allg. Chem.*, 2015, **641**, 304–310.

15 M. Bawohl, P. Schmidt and T. Nilges, *Inorg. Chem.*, 2013, **52**, 11895–11901.

16 M. P. Baumgartner, Dissertation (Dr. rer. nat.), Technische Universität München, 2017.

17 D. Pfister, K. Schäfer, C. Ott, B. Gerke, R. Poettgen, O. Janka, M. Baumgartner, A. Efimova, A. Hohmann, P. Schmidt, S. Venkatachalam, L. van Wuellen, U. Schürmann, L. Kienle, V. Duppel, E. Parzinger, B. Miller, J. Becker, A. Holleitner, R. Weihrich and T. Nilges, *Adv. Mater.*, 2016, **28**, 9783–9791.

18 C. Grotz, M. Köpf, M. Baumgartner, L. A. Jantke, G. Raudaschl-Sieber, T. F. Fässler and T. Nilges, *Z. Anorg. Allg. Chem.*, 2015, **641**, 1395–1399.

19 M. Schöneich, A. Hohmann, P. Schmidt, F. Pielnhofer, F. Bachhuber, R. Weihrich, O. Osters, M. Köpf and T. Nilges, *Z. Kristallogr. - Cryst. Mater.*, 2017, **232**, 91–105.

20 S. Lange, M. Bawohl, R. Weihrich and T. Nilges, *Angew. Chem., Int. Ed.*, 2008, **47**, 5654–5657.

21 A. Utrap, N. Y. Xiang and T. Nilges, *J. Cryst. Growth*, 2017, **475**, 341–345.

22 C. Grotz, K. Schäfer, M. Baumgartner, R. Weihrich and T. Nilges, *Inorg. Chem.*, 2015, **54**, 10794–10800.

23 A. Pfitzner and E. Freudenthaler, *Angew. Chem., Int. Ed.*, 1995, **34**, 1647–1649.

24 D. Regonini, C. R. Bowen, A. Jaroenworaluck and R. Stevens, *Mater. Sci. Eng., R*, 2013, **74**, 377–406.

25 R. Hahn, J. Macak and P. Schmuki, *Electrochem. Commun.*, 2007, **9**, 947–952.

26 P. Kar, Y. Zhang, S. Farsinezhad, A. Mohammadpour, B. D. Wiltshire, H. Sharma and K. Shankar, *Chem. Commun.*, 2015, **51**, 7816–7819.

27 B. M. Rao and S. C. Roy, *J. Phys. Chem. C*, 2013, **118**, 1198–1205.

28 V. Galstyan, A. Vomiero, E. Comini, G. Faglia and G. Sberveglieri, *RSC Adv.*, 2011, **1**, 1038–1044.

29 S. Farsinezhad, A. Mohammadpour, A. N. Dalrymple, J. Geisinger, P. Kar, M. J. Brett and K. Shankar, *J. Nanosci. Nanotechnol.*, 2013, **13**, 2885–2891.

30 S. Farsinezhad, A. N. Dalrymple and K. Shankar, *Phys. Status Solidi A*, 2014, **211**, 1113–1121.

31 X. Chen, M. Schriver, T. Suen and S. S. Mao, *Thin Solid Films*, 2007, **515**, 8511–8514.

32 A. Mohammadpour and K. Shankar, *J. Mater. Chem.*, 2010, **20**, 8474–8477.

33 D. Routkevitch, T. Haslett, L. Ryan, T. Bigioni, C. Douketis and M. Moskovits, *Chem. Phys.*, 1996, **210**, 343–352.

34 Y. Peng, D.-H. Qin, R.-J. Zhou and H.-L. Li, *Mater. Sci. Eng., B*, 2000, **77**, 246–249.

35 D. Xu, X. Shi, G. Guo, L. Gui and Y. Tang, *J. Phys. Chem. B*, 2000, **104**, 5061–5063.

36 M. Lu, M.-K. Li, L.-B. Kong, X.-Y. Guo and H.-L. Li, *Composites, Part B*, 2004, **35**, 179–184.

37 A. Mohammadpour, P. Kar, B. D. Wiltshire, A. M. Askar and K. Shankar, *Curr. Nanosci.*, 2015, **11**, 593–614.

38 N. S. Lewis, *Science*, 2007, **315**, 798–801.

39 X. Zhang, F. Han, B. Shi, S. Farsinezhad, G. P. Dechaine and K. Shankar, *Angew. Chem., Int. Ed.*, 2012, **51**, 12732–12735.

40 D. Zhou, Z. Chen, Q. Yang, C. Shen, G. Tang, S. Zhao, J. Zhang, D. Chen, Q. Wei and X. Dong, *ChemCatChem*, 2016, **8**, 3064–3073.

41 X. Fu, Z. Ji, C. Li and Z. Zhou, *J. Alloys Compd.*, 2016, **688**, 1013–1018.

42 Z. Lou, F. Li, J. Deng, L. Wang and T. Zhang, *ACS Appl. Mater. Interfaces*, 2013, **5**, 12310–12316.

43 P. Qin, M. Paulose, M. I. Dar, T. Moehl, N. Arora, P. Gao, O. K. Varghese, M. Grätzel and M. K. Nazeeruddin, *Small*, 2015, **11**, 5533–5539.

44 U. K. Thakur, R. Kisslinger and K. Shankar, *Nanomaterials*, 2017, **7**, 95.

45 Z. Xiong, H. Wang, N. Xu, H. Li, B. Fang, Y. Zhao, J. Zhang and C. Zheng, *Int. J. Hydrogen Energy*, 2015, **40**, 10049–10062.

46 J. Low, B. Cheng and J. Yu, *Appl. Surf. Sci.*, 2017, **392**, 658–686.

47 E. Üzer, P. Kumar, R. Kisslinger, P. Kar, U. K. Thakur, S. Zeng, K. Shankar and T. Nilges, *ACS Appl. Nano Mater.*, 2019, DOI: 10.1021/acsanm.9b00221.

48 C. Ott, F. Reiter, M. Baumgartner, M. Pielmeier, A. Vogel, P. Walke, S. Burger, M. Ehrenreich, G. Kieslich, D. Daisenberger, J. Armstrong, U. K. Thakur, P. Kumar, S. Chen, D. Donadio, L. S. Walter, R. T. Weitz, K. Shankar and T. Nilges, *Adv. Funct. Mater.*, 2019, **29**, 1900233.